

Volume-based curvature computations illuminate fracture orientations — Early to mid-Paleozoic, Central Basin Platform, west Texas

Charles H. Blumentritt¹, Kurt J. Marfurt¹, and E. Charlotte Sullivan¹

ABSTRACT

Volumetric curvature analysis is a simple but computationally intensive procedure that provides insight into fracture orientation and regional stresses. Until recently, curvature analysis has been limited to computation along horizon surfaces that may be affected by unintentional bias and picking errors introduced during the interpretation process. Volumetric curvature is best estimated in a two-step process. In the first step, we use a moving-analysis subvolume to estimate volumetric reflector dip and azimuth for the best-fit tangent plane for each sample in the full volume. In the second step, we calculate curvature from adjacent measures of dip and azimuth. We use larger curvature analysis windows to estimate longer wavelength curvatures. Such a technique allows us to output full 3D volumes of curvature values for one or more scales of analysis. We apply these techniques to a data set from the Central Basin Platform of west Texas and find lineaments not observable with other seismic attributes. These lineaments indicate that, in the lower Paleozoic interval, a left-lateral shear couple oriented due east-west controls the local stress regime. Such a model predicts that extension faulting and fractures will be oriented northeast-southwest. The example demonstrates the potential of this new technology to determine stress regimes and predict azimuths of open fractures.

INTRODUCTION

This geologic curvature analysis is based on the principle that stresses applied to an area will result in predictable orientations of fractures, folds, and faults related to the orientations of the three principal stresses (Harding, 1974). The basic relation has been calibrated through surface studies from field mapping (e.g. Murray, 1968; Lisle, 1994) and air photo analysis (McQuillan, 1974). In the

subsurface, stress analysis must be done by integrating surface trends with well and seismic data control (e.g., Ward and Beeson, 2004, personal communication). In this workflow, the interpreter generates a map of some identifiable geologic horizon and analyzes the map for areas of anomalous curvature. Then, using an appropriate geologic model, the interpreter relates curvature to regional or local stresses.

According to Roberts (2001), curvature at any point on a 2D section is the inverse of the radius of a circle whose circumference approximates the surface at that point (Figure 1). In the case of a 3D surface, curvature is calculated by passing a quadratic surface through a grid of nine or more data points. By successively low-pass-filtering such an interpreted map, Sigismondi and Soldo (2003) obtained longer wavelength curvature estimates. Bergbauer et al. (2003) calculated long wavelength estimates of curvature through a more direct Fourier (k_x, k_y) decomposition of an interpreted horizon. Al-Dossary and Marfurt (2006) extended these ideas to generate spectral estimates of curvature for an entire seismic volume by use of an (x, y) operator implementation of a (k_x, k_y) bandpass filter. Such an operator avoids the need to transpose the seismic dip and azimuth cubes and runs in parallel on an inexpensive computer cluster environment.

Geologists have been using curvature analysis in the petroleum industry for at least 35 years (e.g., Murray, 1968) to identify local areas of increased bending of rock units for the purpose of locating zones of increased fracturing and improved production. Lisle (1994) revisited the area studied by Murray (1968) and gave a more detailed analysis of the curvature of the structure, finding that areas of high magnitudes of Gaussian curvature correlate with areas of greater deformation and therefore greater density of fractures. He further indicated that faulting creates intense fracturing and thus may be identifiable by areas of high magnitudes of Gaussian curvature. More recently, Bergbauer et al. (2003) used maximum curvature to locate faults along a horizon in the North Sea. Massaferro et al. (2003) used maximum-curvature analysis on structures in Argentina to delineate structural trends and identify fracture zones. They found that the fractures observed on a vertical image log in one well were consis-

Manuscript received by the Editor July 13, 2004; revised manuscript received January 17, 2006; published online September 7, 2006.

¹Allied Geophysical Laboratories, University of Houston Room 510 Science and Research Building 1, Cullen Road Entrance 14 Houston, Texas 77204. E-mail: cblumentritt@geo-texture.com; kmarfurt@uh.edu; charlotte.sullivan@pnl.gov.

© 2006 Society of Exploration Geophysicists. All rights reserved.

tent in direction and intensity with the amount of fracturing predicted by the curvature technique. Sigismondi and Soldo (2003) showed examples of curvature analysis assisting in the interpretation of structures in Argentina. They found that maximum curvature highlights fault trends and sense of faulting and that most negative curvature delineates subtle lineaments within fault blocks. Hart et al. (2002) analyzed production data and showed that the intersection of curvature (change in dip) trends directly correlated with the better performing wells. In most cases, these workers limited their analyses to a single type of curvature.

In this paper, we begin with a review of the definition, calculation, and interpretation significance of the various curvature estimates. In the next section, we summarize the tectonic and depositional framework of the survey area, as well as the major features seen on the seismic data and attribute volumes, including volumetric curvature. Finally, we use these new attributes to predict the stress field at the time of structural deformation.

CURVATURE

Curvature of a surface at a particular point is the inverse of a circle's radius which is tangent to that surface at that point (Roberts,

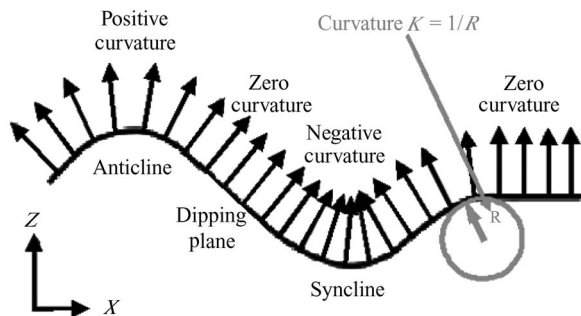


Figure 1. Curvature in two dimensions. Note that curvature is defined as the inverse of the radius of a circle that is tangent to the surface at any point and that, by convention, positive curvature is concave downward, and negative curvature is concave upward (after Roberts, 2001).

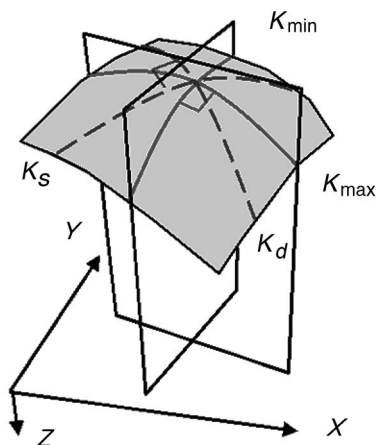


Figure 2. Curvature in three dimensions, showing maximum curvature k_{max} , minimum curvature k_{min} , dip curvature k_{dip} , and strike curvature k_{str} . Not shown are Gaussian curvature k_g , mean curvature k_{mean} , most positive curvature k_{pos} , and most negative curvature k_{neg} (from Roberts, 2001; after Sigismondi and Solda, 2003).

2001). For our purposes, we will be concerned with circles in a plane normal to the surface and will consider positive curvature to be concave downward (Figure 1). Roberts (2001) gives a very readable discussion of the various types of curvature and other related attributes, based on work initially done by Gauss in the 1820s. He found that numerous types of curvature could be determined at every point on a gridded surface by fitting a quadratic surface to the data and using the coefficients of the quadratic equation. At any given point on a surface, there are an infinite number of circles in normal planes of different azimuths that may be tangent to the surface. For a quadratic surface, the curvature of the tangent circle with the smallest radius in a normal plane is called the maximum curvature, k_{max} . The curvature of the tangent circle in the normal plane perpendicular to this has the minimum curvature, k_{min} .

Together, these two curvatures are known as the principal curvatures and, along with the azimuth of k_{min} , completely define the quadratic surface. From k_{min} and k_{max} , we may compute the Gaussian curvature k_g as the product of the two principal curvatures and the mean curvature k_{mean} as their average. Other important curvatures are the most positive k_{pos} , most negative k_{neg} , dip k_{dip} , and strike k_{strike} curvatures. (See Figure 2 and Roberts, 2001, for more detailed descriptions of these.) Other attributes derivable in this analysis include curvedness, which is equal to $(k_{max}^2 + k_{min}^2)^{1/2}$; the shape index, which indicates the local morphological structure of the surface (dome, ridge, plane, valley, bowl, or saddle); and rotation, which measures scissors-like deformation not represented by our smooth quadratic surfaced model.

Several of these curvatures give information about the morphology of the surfaces from which they are extracted, as can be visualized by extending the curved line in Figure 1 infinitely into and out of the page. Such a structure is the result of folding an initially flat surface around axes perpendicular to the page (Lisle, 1994). It is intuitively evident that there is no deformation of the surface perpendicular to the page and varying amounts of deformation along the curved line. At every point along the curved line or any other line on the surface parallel to the line, the minimum curvature will be perpendicular to the page and will be zero. However, the maximum curvature will vary between a large positive value at the peak of the anticline through zero to a large negative value at the trough of the syncline. In this case, the Gaussian curvature, which is the product of the maximum and minimum curvatures, will be zero at all points on the surface. Maximum curvature, as noted above, will vary along the curved line but will be constant perpendicular to it.

Therefore, a color-coded map view of the maximum curvature of this surface will consist of a series of color bands perpendicular to the page, with bands representing the maximum positive value along the anticlinal axes and bands representing the maximum negative values along the synclinal axes. Faulting may be represented in the same manner by envisioning a break and offset in either a normal or reverse orientation between the anticline and the syncline and running perpendicular to the page. The anticline and syncline will then represent drag in the upthrown and downthrown blocks of the fault, respectively. The preceding descriptions will be true whenever the surface dips in a linear manner into and out of the page.

In the above visualization, if the extension of the curved line into and out of the page is not linear but rather curves downward in both directions, then the minimum curvature and the Gaussian curvature will no longer be zero. There will be deformation perpendicular to the page, and the surface cannot be formed by simple cylindrical folding of an initially flat surface but requires warping of that sur-

face. Therefore, nonzero Gaussian curvature indicates that a surface has been warped. The greatest amount of total deformation is likely to be associated with areas of greatest absolute Gaussian curvature.

In the above discussions, the maximum curvature is the signed value of the largest absolute curvature at each point. Curvatures that are more sensitive to the sign are the most positive curvature and the most negative curvature. In the second case described above, in which the surface dips downward away from the page on each side of the page, the most negative curvature at the syncline will be parallel to the page, and the most positive curvature will be perpendicular. At the anticline, as illustrated in Figure 2, curvature at all azimuths is positive. The most positive curvature will be parallel to the page, and the most negative curvature, which in this case would be the least positive curvature, will be perpendicular to the page. Map views of color-coded most positive curvature, especially if values less than zero are omitted, will show anticlinal axes only, and map views of color-coded most negative curvature with the positive values omitted will show synclinal axes.

Roberts (2001), Massaferro et al. (2003), and Sigismondi and Soldo (2003) conducted their analyses on gridded surfaces interpreted from 3D seismic surveys. The use of such regularly sampled surfaces permits rapid calculation of curvatures for every point on such surfaces but introduces three problems. First, even the most optimally processed seismic data contain some noise that will affect the curvature computations. Second, such an interpretation by its very nature will have some influence or bias introduced by the interpreter. Finally, the grid spacing of the surface controls the scale at which the analysis is done.

Bergbauer et al. (2003) present the fractal nature of curvature from sand grains to continental bulges as well as the effects of noise on curvature calculations from a surface picked from a 3D seismic volume. Their solutions — as well as those of Roberts (2001) and other authors — to the first and third problems are to smooth or otherwise filter the surface being investigated to remove noise and to vary the grid spacing to precondition the surface to illuminate curvature at a particular wavelength. None of the authors discusses a solution for interpreter bias.

Al Dossary and Marfurt (2006) avoid the interpreter bias problem by calculating curvature at every point in the seismic volume. In their method, the moving subvolume used for computation provides sufficient averaging in the lateral and vertical directions to provide smoothly varying results on a local basis. We then display curvature extractions along rather than curvature calculations of a horizon. Such volumetric curvature calculations also are amenable to 3D visualization including animation, opacity analysis, and voxel picking. We address the problem of accurately determining local geologic dip without bias or noise effects through the use of a multiwindow estimation of dip and azimuth (Marfurt, 2006) that is based on a finite temporal window (containing 11 samples in this study) rather than the single-sample peak or trough estimates used in map analysis. We output the dip and azimuth from the analysis in the format of inline and crossline dip for each sample in the volume. Finally, we calculate curvature at each sample at various wavelengths using a fractional derivative of the dip vector (al Dossary and Marfurt, 2006) and the equations provided by Roberts (2001).

WEST TEXAS EXAMPLE

Geologic setting

The Permian Basin of west Texas and eastern New Mexico (Figure 3) is a world-class petroleum province that has been studied in detail for well over half a century (Galley, 1958; Frenzel et al., 1988). A key feature of this basin is the buried Central Basin Platform (CBP) that gives evidence the pre-Mesozoic may be divided into two gross intervals. First, the lower-to-middle Paleozoic interval records subsidence and deposition of shelfal to basinal deposits that ended with Mississippian to Pennsylvanian-age tectonism that uplifted the CBP. Second, the Permian interval records gentle subsidence with little large-scale deformation. Thus, the Pennsylvanian and older interval is effectively decoupled from the later section, has no surface expression, and can be studied only through well and seismic data (Figure 4).

The nature of the pre-Permian tectonics is enigmatic. The older part of the stratigraphic section, such as the Ordovician, has as much as 10,000 ft (3000 m) of vertical relief along the western side of the CBP (Frenzel, 1988), and the platform was initially interpreted to be the result of vertical tectonics. Harrington (1963) observed the orientations of the oilfield structures and the vertical nature of faulting and proposed that there is a component of right lateral faulting associated with the CBP. Gardiner (1990) divided the area into six

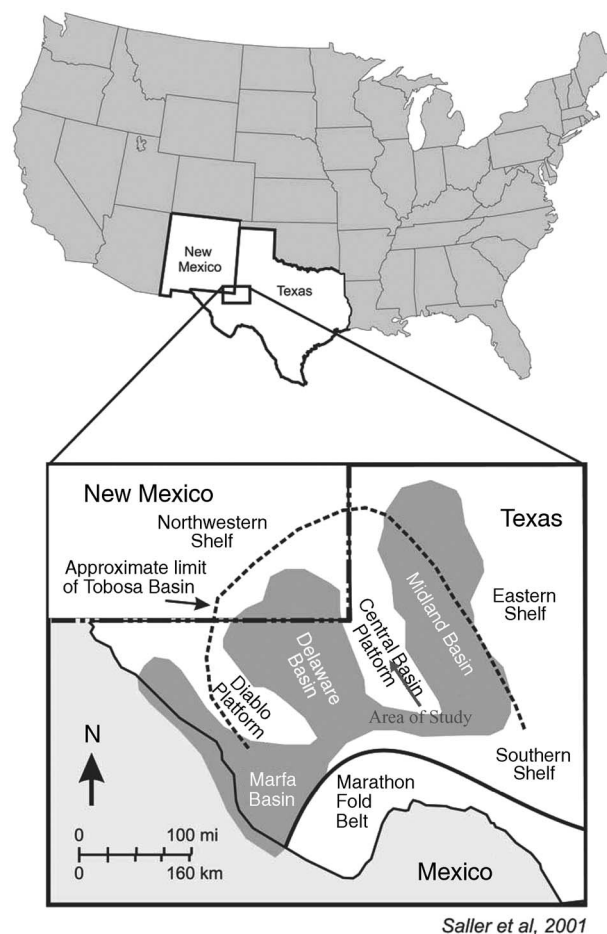


Figure 3. Location of the Permian Basin and Central Basin Platform of west Texas and eastern New Mexico (after Saller et al., 2001).

blocks, each with a different tectonic nature, with the southern part of the CBP affected by left lateral wrenching and the northern part by right lateral wrenching. Shumaker (1992) recognized the same six blocks and found them to be separated by trends of east-west left lateral faulting that cross the platform. He indicated that such movement and the clockwise rotation of the intervening blocks are the result of a basin-scale left-lateral shear couple applied to the entire platform. Yang and Dorobek (1995) commented that clockwise rota-

tion of blocks would have to be created by right lateral faulting, and they related the formation of rotational blocks observed by Shumaker (1992) to right lateral movement along the roughly north-south-trending bounding faults along either side of the platform. They divided the platform into two blocks: the Fort Stockton Block of Gardiner (1990) and Shumaker (1992) in the southwest and the larger Andector Block in the north and east (Figure 5). They stated that their interpretation was regional in nature and did not describe any specific area in detail. The goal of this paper is to evaluate these hypotheses by applying our new suite of curvature attributes to a 3D seismic survey located along the Fort Stockton-Andector boundary.

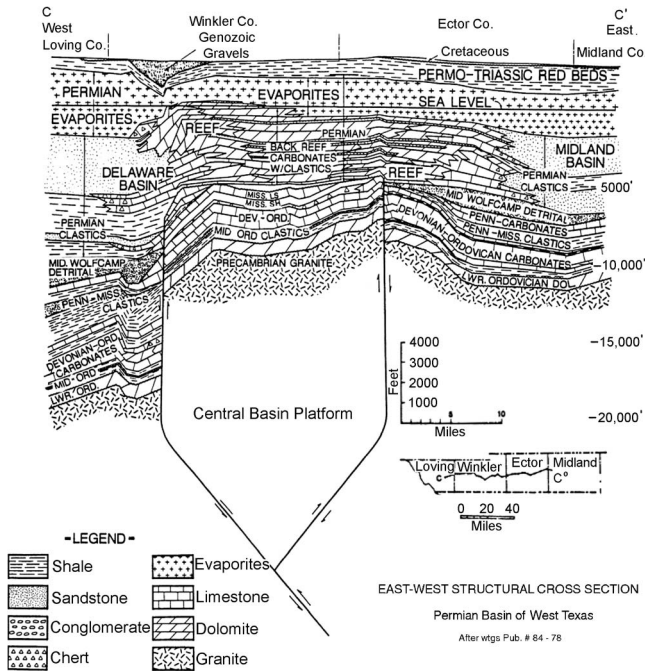


Figure 4. Cross section of Central Basin Platform, showing decoupling of pre-Permian and Permian sections (from Feldman, 1989).

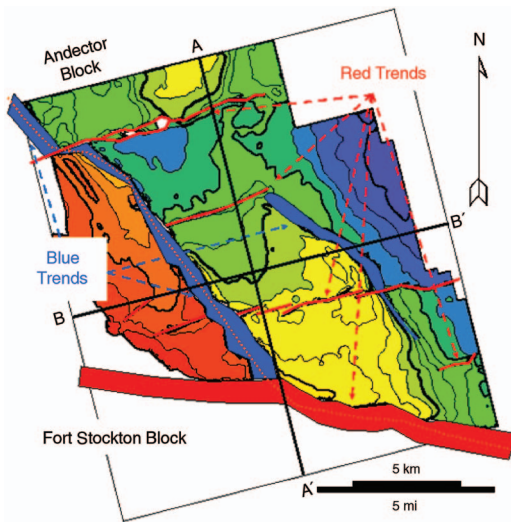


Figure 5. Devonian structure map from the study area. Note the east-northeast–west-southwest-trending red faults and the northwest-southeast-trending blue faults. The red faults show virtually no horizontal separation whereas the blue faults show substantial horizontal separation. Lines A and B are discussed in Figures 6 and 7, respectively.

Curvature analysis

Our data set was acquired over the southern part of the CBP along the boundary between the Fort Stockton and Andector blocks and covers an area of 18.8 by 17.6 km (11.7 by 10.9 miles) with an inline and crossline spacing of 33.5 m (110 ft). The subvolume size for the dip and azimuth computations was 3 × 3 seismic traces by 20 ms (11 samples) chosen from five laterally overlapping windows. The long wavelength estimates of curvature were calculated from these dip and azimuth estimates using a 21 × 21 seismic trace by one-sample analysis window. Al Dossary and Marfurt (2006) discuss this methodology in detail.

Figure 5 shows a time structure map at the top of the Devonian Thirty-one Formation. Two sets of nearly orthogonal faults are present in the data, with the east-northeast–west-southwest faults (the red faults) having a relatively narrow fault trace and the north-northwest–south-southeast faults having a much broader fault trace. The narrow and vertical fault traces of the ENE–WSW faults are evident on line AA', running northwest-southeast, shown in Figure 6. This geometry, along with offsets of linear features across those faults, strongly suggests that these are left-lateral wrench faults. The broader fault trace and apparent repeat section of the northwest-southeast faults, which we call the blue faults, are evident on Figure 7, which runs west-southwest–east-northeast through the middle of the data set. These blue faults are actually zones of complex interaction because there is some evidence of re-versal of direction of throw in the vertical direction and because the width of the disturbed zone is approximately three times the vertical separation across it.

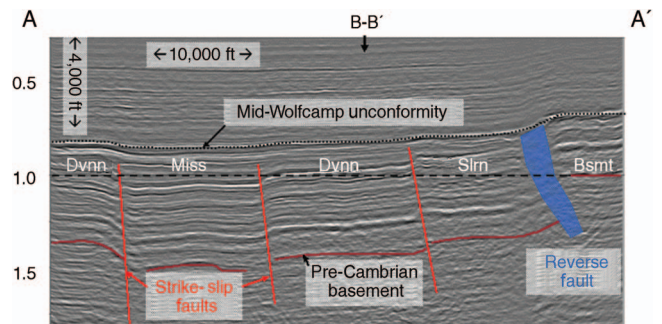


Figure 6. Seismic line AA' showing tectonically active early-to-middle Paleozoic separated from tectonically quiescent Permian and younger. Note also the vertical nature and narrow trace of the strike slip faults (red faults). Time slices shown in Figures 8–10 are taken along the 1.000 s timing line. This section shows that the time slices cut across multiple stratigraphic levels, the various fault blocks are relatively flat, and the fault blocks step down from south to north. Vertical exaggeration is approximately 2.5:1.

In Figure 8, we display a time slice through the seismic data volume that shows the major trends, especially the broad zones of the blue faults and, to a lesser degree, the narrow fault traces of the red faults. The rocks represented by this slice and the other attribute slices (Figures 8–10) are all below the mid-Wolfcamp unconformity that separates the lower Paleozoic section from the Permian and younger section. Inspection of Figures 6 and 7 shows that within a fault block, the structure is relatively flat so that locally the time slices represent horizon slices. Immediately evident on these slices is the rhombic nature of the two central blocks, suggesting left lateral wrenching but not the block rotation of Shumaker (1992). However, these rhomboids do not indicate transtension because the blocks are not low areas; rather, they step down progressively from east to west and south to north.

Figure 9 shows a time slice of the coherence attribute at the same level seen in Figure 8. As might be expected, the coherence attribute shows better definition of the fault trends seen on the conventional data (Figure 8) and brings out additional information, such as faults not seen on the conventional data and potential stratigraphic features.

Figure 10 shows the Gaussian maximum, most positive, and most negative curvature attributes at the same time as the slices in Figures 8 and 9. Gaussian curvature (Figure 10a) has positive values, indicating maximum curvature and minimum curvature have the same sign (in red) and negative values (in green). Local anomalies occur within fault zones visible on other displays but do not show any alignments. Cylindrical folding, which would produce linear trends, has a minimum-curvature value of zero, thus causing the Gaussian curvature to be zero. The maximum curvature (Figure 10b) shows positive curvature, indicating anticlinal axes (in red) and negative curvature, indicating synclinal axes (in green). In many areas, axes of different polarity appear together, suggesting the anticline/syncline or upthrown/downthrown pairs described earlier. In other areas, isolated axes of one polarity or the other appear. The large number of such axes along with numerous parallel trends make it difficult to identify uniquely the features creating the patterns.

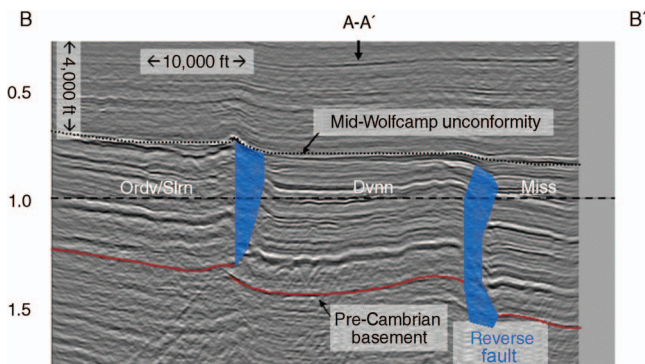


Figure 7. Seismic line BB', showing reverse nature and broad trace of NW-SE trending reverse faults (blue faults). Time slices shown in Figures 8–10 are taken along the 1.000 s timing line. This section shows that the time slices cut across multiple stratigraphic levels, the various fault blocks are relatively flat, and the fault blocks step down from west to east. Vertical exaggeration is approximately 2.5:1

In contrast, the most positive curvature (Figure 10c) shows fewer lineaments and isolates each one from the others to permit easier identification and interpretation. Figure 10d shows that the most negative-curvature attribute is very similar to the most positive curvature, but close inspection shows that the locations of the lineaments have shifted, corresponding to the offset of the axes in an anticline/syncline pair. Interpretation of the most negative curvature

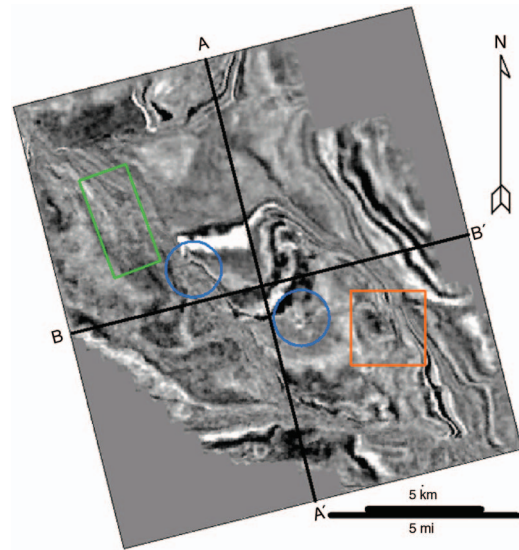


Figure 8. Time slice of conventional seismic data volume at 1.000 s. Significance of areas highlighted by geometric figures is discussed in Figure 9.

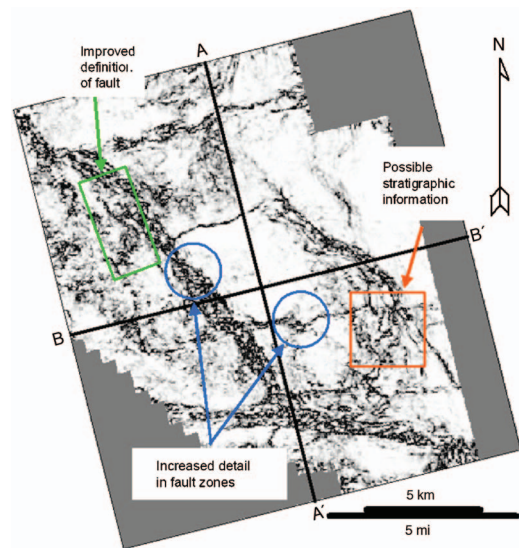


Figure 9. Time slice of coherence attribute volume at same travel-time as shown in Figure 8. Note that the broad zones of the north-west-south-east-trending faults shows up better and with increased detail on the coherence attribute. Note also the rhomboid character of the block in the center of the image. This is not a pullapart basin because the faults step down from south and west to north and east as indicated in Figures 6 and 7. Blue circles indicate areas of improved detail in fault trends versus conventional data; green rectangle indicates improved definition of fault, and orange square indicates area of illumination of possible stratigraphic features.

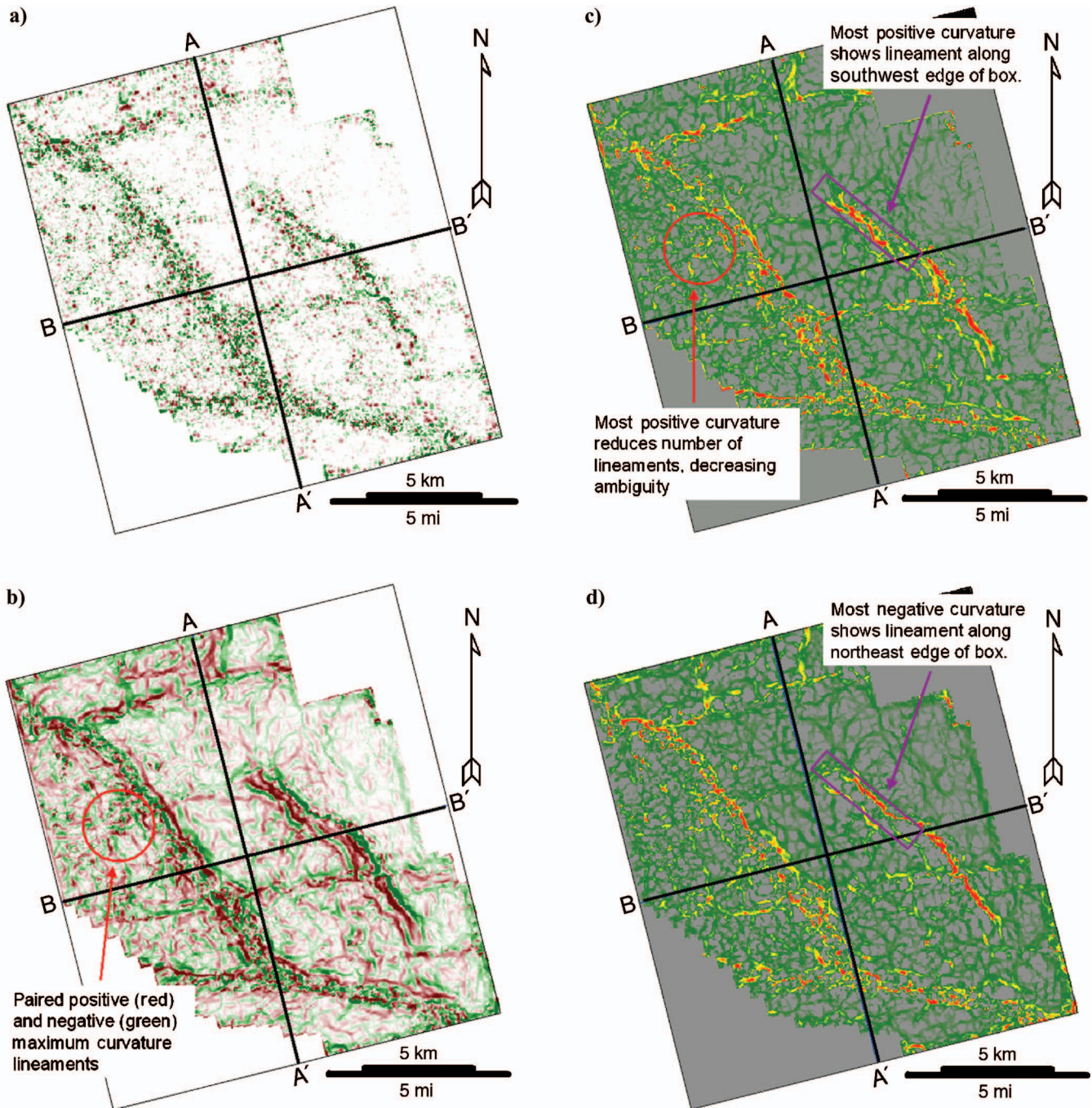


Figure 10. Comparison of curvature attributes. (a) Gaussian curvature; red indicates high positive values; green indicates high negative values. Plot shows detail in fault zones visible on amplitude and coherence data, but little detail within fault blocks. (b) Maximum curvature. Red indicates large positive values, and green indicates large negative values. Parallel trends of positive and negative (red circle) values indicate anticline/syncline pairs. Large number of trends increase complexity of interpretation. (c) Most positive curvature. Red indicates large positive values; gray indicates values less than or equal to zero. Parallel trends (red circle) replaced by positive trends only, decreasing number of lineaments and reducing ambiguity in interpretation. Purple box shows strong positive curvature trend, indicating drag in upthrown fault block. (d) Most-negative curvature. Red indicates large negative values; gray indicates values greater than or equal to zero. This is very similar to most positive curvature, except that trends are laterally displaced. Purple box shows strong negative curvature indicating drag in downthrown fault block. This trend is shifted northeast from the same trend shown in (c). Analyses of most-positive curvature and most-negative curvature should produce identical results. See text for additional discussion.

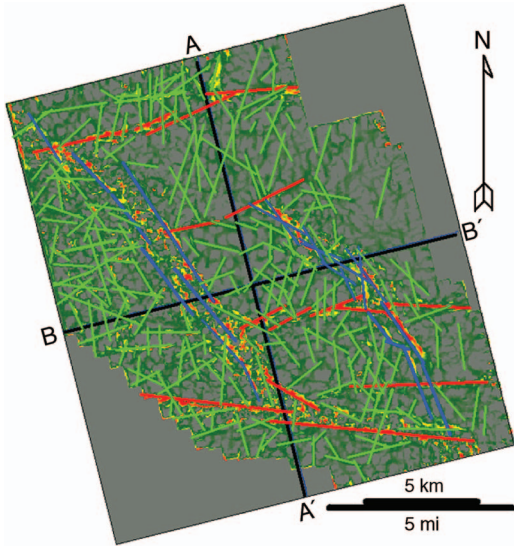


Figure 11. Time slice through most positive curvature volume with interpreted lineaments posted. This figure compares to Figure 10c. Red indicates high curvature; gray indicates low curvature. Note the improved delineation in the broad zones of the blue faults as well as the illumination of lineaments within the fault blocks on the most positive curvature attribute. Red and blue lineaments represent trends previously observed and discussed. Green lineaments represent trends visible only on curvature attribute.

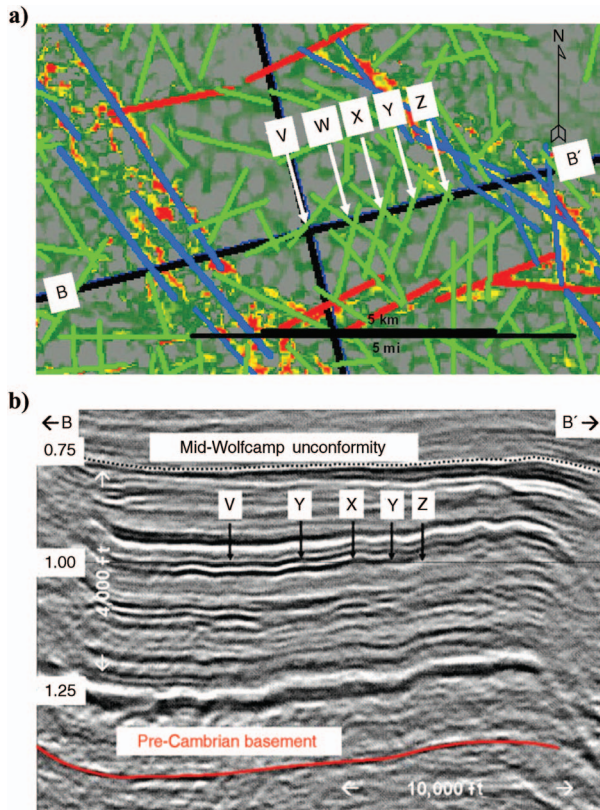


Figure 12. Enlarged views of (a) most positive curvature time slice and (b) line BB' showing locations of five lineaments, indicated by arrows visible on the most positive curvature slice. Red indicates high curvature; gray indicates low curvature. Lineaments appear to be associated with undulations on seismic section but tie to different positions on different undulations.

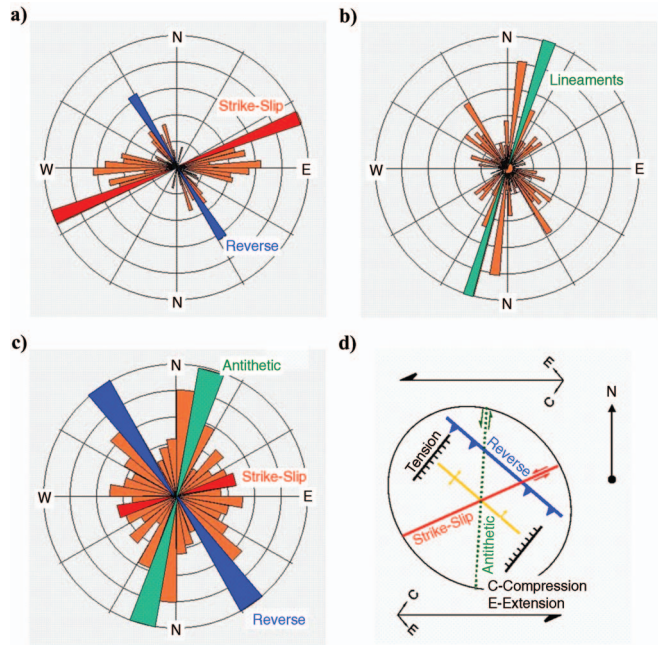


Figure 13. Rose diagrams of lineaments interpreted from most positive curvature attribute. (a) Red and blue trends that correspond to faults observable on all presentations of the seismic data; (b) green trends that correspond to lineaments that are observable only on most positive curvature attribute. The most frequently occurring azimuth does not correspond to any observed for the red and blue trends. The second most frequently occurring azimuth does align with the most often occurring azimuth for the blue trend. (c) All lineaments with the most frequently occurring azimuths for the primary trends highlighted; (d) a left lateral strain ellipsoid (modified from Harding, 1974) with the primary trends highlighted. In a–c, highlighted trends are color coded to match red, blue, and green trends discussed in text. This model suggests that tension fractures are oriented along a strike of N40–45°E.

should produce essentially identical results to interpretation of the most positive curvature, and the choice between them is arbitrary.

Figure 11 shows the most-positive curvature (K_{pos}) slice of Figure 10c with lineaments posted. The red and blue faults are still evident, with greater detail present in the broad zones of the blue faults, but a new level of lineaments — the green trend — is evident.

Figure 12 shows enlargements of the most positive curvature time slice (Figure 11a) and a portion of line B-B' (Figure 11b) with five corresponding green trend lineaments indicated on each by arrows. Four of the lineaments, V, W, X, and Y, have a northeasterly strike and the fifth, Z, a northwesterly strike. Although all five seem to be related to an undulating reflection on the seismic section, they fall at different positions of individual waves along that horizon.

Next, we computed the azimuths and lengths of all of the lineaments picked on the most positive curvature time slice (Figure 11) and plotted them in rose diagrams. Figure 13a shows the rose diagram of just the red and blue trends because these are readily observable on all representations of the data. As expected, they show nearly orthogonal trends. Figure 13b shows the azimuths of the green lineaments, and these tend to be somewhat bimodal, with the main trend lying between those of the red and blue faults and a secondary trend lying along the same trend as the blue faults. Figure 13c shows a rose diagram of all lineaments, and Figure 13d shows Harding's (1974)

strain ellipsoid for a left and right lateral shear couple. The observed faults fit the left lateral shear couple model with the shear couple aligned in a due east-west orientation. In that case, the expected primary shears correspond to the red faults and, as expected, the reverse fault trend corresponds to the blue faults. Using this model, the green lineaments correspond to the antithetic strike slip trend. This model (Harding, 1974) further predicts that extensional trends (mode 1, or open, fractures) will be oriented N40–45°E.

CONCLUSION

We have introduced a new volume-based method of evaluating stress regimes and predicting azimuths of open fractures. We build on a proven method of analyzing geologic structures by computing curvatures at each sample of a 3D seismic volume and outputting those curvatures as additional seismic volumes that may be sliced along time slices or interpreted horizons. Initial results of the application of this methodology to a data set from the CBP in west Texas indicate that analysis of these curvature volumes leads to structural interpretations that are consistent with the fault patterns but not the block rotation. These structural interpretations explain observed geologic features and predict stress regimes and directions of extensional fractures.

Most positive curvature (or most negative curvature) provides a more detailed and less ambiguous attribute for defining subtle lineaments related to regional or local stresses than the more commonly used Gaussian- and maximum-curvature attributes. This technique should be applicable in all terranes.

Our new method of calculating curvature provides a powerful tool for field- and basin-scale analysis of stress regimes and orientation of tension fractures. These findings have broad implications for exploration, development, and management of fractured reservoirs.

ACKNOWLEDGMENTS

The authors gratefully acknowledge Occidental Permian, Ltd., BP Americas, and Tobin for their data contributions and the state of Texas for funding through their Advanced Technology Program grant. We also acknowledge Core Laboratories for permission to display data processed with Coherence technology.

REFERENCES

- al Dossary, S., and K. J. Marfurt, 2006, 3-D volumetric multispectral estimates of reflector curvature and rotation: *Geophysics*, this issue.
- Bergbauer, S., T. Mukerji, and P. Hennings, 2003, Improving curvature analyses of deformed horizons using scale-dependent filtering techniques: *AAPG Bulletin*, **87**, 1255–1272.
- Feldman, M. L., 1989, Paleozoic framework of the Gulf of Mexico, *in* J. E. Flis, R. C. Price, and J. F. Sarg, eds., *Search for the subtle trap: Hydrocarbon exploration in mature basins: West Texas Geological Society Publication 89–85*, 199–209.
- Frenzel, H. H., R. R. Bloomer, R. B. Cline, J. M. Cys, J. E. Galley, W. R. Gibson, J. H. Hills, W. E. King, W. R. Seager, F. E. Kottlowski, S. Thompson, III, G. C. Luff, B. T. Pearson, and D. C. Van Sclen, 1988, The Permian Basin region, *in* L. L. Sloss, ed., *Sedimentary cover — North American Craton: Geological Society of America, The Geology of North America, D-2*, 261–306.
- Galley, J. E., 1958, Oil and geology in the Permian Basin of Texas and New Mexico, *in* L. G. Weeks, ed., *Habitat of oil: AAPG*, 395–446.
- Gardiner, W. B., 1990, Fault fabric and structural subprovinces of the Central Basin Platform: A model for strike-slip movement, *in* J. E. Flis and R. C. Price, eds., *Permian Basin oil and gas fields: Innovative ideas in exploration and development: West Texas Geological Society Publication*, 90–87, 15–27.
- Harding, T. P., 1974, Petroleum traps associated with wrench faults: *AAPG Bulletin*, **58**, 1290–1304.
- Harrington, J. W., 1963, Opinion of structural mechanics of Central Basin Platform area, west Texas: *AAPG Bulletin*, **47**, 2023–2038.
- Hart, B. S., R. Pearson, and G. C. Rawling, 2002, 3-D seismic horizon-based approaches to fracture-swarm sweet spot definition in tight-gas reservoirs: *The Leading Edge*, **21**, 28–35.
- Lisle, R. J., 1994, Detection of zones of abnormal strains in structures using Gaussian curvature analysis: *AAPG Bulletin*, **78**, 1811–1819.
- Marfurt, K. J., 2006, Robust estimates of reflector dip and azimuth: *Geophysics*, **71**, this issue.
- Masaferro, J. L., M. Bulnes, J. Poblet, and M. Casson, 2003, Kinematic evolution and fracture prediction of the Valle Morado structure inferred from 3-D seismic data, Salta Province, northwest Argentina: *AAPG Bulletin*, **87**, 1083–1104.
- McQuillan, H., 1974, Fracture patterns on Kuh-e Asmari anticline, southwest Iran: *AAPG Bulletin*, **58**, 236–246.
- Murray, Jr., G. H., 1968, Quantitative fracture study-Spanish Pool, McKenzie County, North Dakota: *AAPG Bulletin*, **52**, 57–65.
- Roberts, A., 2001, Curvature attributes and their application to 3D interpreted horizons: *First Break*, **19**, 85–100.
- Saller, A., B. Ball, S. Robertson, B. McPherson, C. Wene, R. Nims, and J. Gogas, 2001, Reservoir characteristics of Devonian cherts and their control on oil recovery; Dollarhide field, west Texas: *AAPG Bulletin*, **85**, 35–50.
- Shumaker, R. C., 1992, Paleozoic structure of the Central Basin Uplift and adjacent Delaware Basin, West Texas: *AAPG Bulletin*, **76**, 1804–1824.
- Sigismondi, M. E., and J. C. Soldo, 2003, Curvature attributes and seismic interpretation: Case studies from Argentina Basins: *The Leading Edge*, **23**, 1122–1126.
- Yang, K.-M., and S. L. Dorobek, 1995, The Permian Basin of West Texas and New Mexico: Tectonic history of a “composite” foreland basin and its effects on stratigraphic development, *in* S. L. Dorobek and G. M. Ross, eds., *Stratigraphic evolution of foreland basins: SEPM Special Publication 52*, 149–174.